AGU PUBLICATIONS

JGR

Journal of Geophysical Research: Space Physics

RESEARCH ARTICLE
10.1002/2017JA024524

Special Section:
Magnetospheric Multiscale (MMS) mission results throughout the first primary mission phase

Electron Dynamics Within the Electron Diffusion Region of Asymmetric Reconnection

M. R. Argall[1], K. Paulson[1], L. Alm[1], A. Rager[2], J. Dorelli[2], J. Shuster[2], S. Wang[2], R. B. Torbert[1,3], H. Vaith[1], I. Dors[1], M. Chutter[1], C. Farrugia[1], J. Burch[3], C. Pollock[2], B. Giles[2], D. Gershman[2], B. Lavraud[4], C. T. Russell[5], R. Strangeway[5], W. Magnes[6], P.-A. Lindqvist[7], Yu. V. Khotyaintsev[8], R. E. Ergun[9], and N. Ahmadi[9]

[1]Space Science Center, University of New Hampshire, Durham, NH, USA, [2]NASA Goddard Space Flight Center, Greenbelt, MD, USA, [3]Southwest Research Institute, San Antonio, TX, USA, [4]Institut de Recherche en Astrophysique et Planétologie, CNRS, UPS, Université de Toulouse, France, [5]Earth, Planetary, and Space Sciences, University of California, Los Angeles, CA, USA, [6]Space Research Institute, Austrian Academy of Sciences, Graz, Austria, [7]KTH Royal Institute of Technology, Stockholm, Sweden, [8]Swedish Institute of Space Physics, Uppsala, Sweden, [9]University of Colorado Boulder, Boulder, CO, USA

Abstract We investigate the agyrotropic nature of electron distribution functions and their substructure to illuminate electron dynamics in a previously reported electron diffusion region (EDR) event. In particular, agyrotropy is examined as a function of energy to reveal detailed finite Larmor radius effects for the first time. It is shown that the previously reported ~66 eV agyrotropic "crescent" population that has been accelerated as a result of reconnection is evanescent in nature because it mixes with a denser, gyrotopic background. Meanwhile, accelerated agyrotropic populations at 250 and 500 eV are more prominent because the background plasma at those energies is more tenuous. Agyrotropy at 250 and 500 eV is also more persistent than at 66 eV because of finite Larmor radius effects; agyrotropy is observed 2.5 ion inertial lengths from the EDR at 500 eV, but only in close proximity to the EDR at 66 eV. We also observe linearly polarized electrostatic waves leading up to and within the EDR. They have wave normal angles near 90°, and their occurrence and intensity correlate with agyrotropy. Within the EDR, they modulate the flux of 500 eV electrons travelling along the current layer. The net electric field intensifies the reconnection current, resulting in a flow of energy from the fields into the plasma.

Plain Language Summary The process of reconnection involves an explosive transfer of magnetic energy into particle energy. When energetic particles contact modern technology such as satellites, cell phones, or other electronic devices, they can cause random errors and failures. Exactly how particles are energized via reconnection, however, is still unknown. Fortunately, the Magnetospheric Multiscale mission is finally able to detect and analyze reconnection processes. One recent finding is that energized particles take on a crescent-shaped configuration in the vicinity of reconnection and that this crescent shape is related to the energy conversion process. In our paper, we explain why the crescent shape has not been observed until now and inspect particle motions to determine what impact it has on energy conversion. When reconnection heats the plasma, the crescent shape forms from the cool, tenuous particles. As plasmas from different regions mix, dense, nonheated plasma obscures the crescent shape in our observations. The highest-energy particle population created by reconnection, though, also contains features of the crescent shape that are more persistent but appear less dramatically in the data.

Key Points:
- We study agyrotropy and energy dissipation in an EDR event on the ion and electron inertial scales
- Agyrotropy is observed 2.5 ion inertial lengths from the X point at energies above the electron crescent population
- Amplitude and occurrence of electrostatic, linearly polarized waves near f_{ce} correlate with increased agyrotropy in and around the EDR

Correspondence to:
M. R. Argall,
matthew.argall@unh.edu

Citation:
Argall, M. R., Paulson, K., Alm, L., Rager, A., Dorelli, J., Shuster, J., … Ahmadi, N. (2018). Electron dynamics within the electron diffusion region of asymmetric reconnection. *Journal of Geophysical Research: Space Physics*, *123*, 146–162. https://doi.org/10.1002/2017JA024524

Received 27 JUN 2017
Accepted 5 DEC 2017
Accepted article online 20 DEC 2017
Published online 4 JAN 2018

©2017. American Geophysical Union. All Rights Reserved.

1. Introduction

Magnetic reconnection is one of the main mechanisms responsible for the energization and transport of plasmas throughout the universe. At Earth's magnetopause (MP), oppositely directed field lines from the magnetosheath (MSH) and magnetosphere (MSP) diffuse through the ion plasma at large scales, and electron plasma at small scales, dissipating energy as field lines break and reconnect. It is at small scales, in the electron diffusion region (EDR), where kinetic processes that govern reconnection manifest themselves. Thus, understanding electron heating and acceleration in the EDR is key to unravelling larger energy conversion and transport processes.

Electron energization during symmetric reconnection, as in the magnetotail where the plasma and magnetic field conditions are equal on either side of the reconnection site, occurs in two general locations: the diffusion region and the flux pileup region. As electrons drift through the ion diffusion region toward the reconnection site, they become trapped in and accelerated by a potential well parallel to the magnetic field (Egedal, Lê, Katz, et al., 2010; Egedal, Lê, Zhu, et al., 2010; Graham et al., 2014). Upon entering the current layer, their gyromotion causes them to meander across the magnetotail while being accelerated by the reconnection electric field (Fu et al., 2006, Huang et al., 2010; Speiser, 1965). An inversion electric field and a phase space hole form surrounding the X line (Chen et al., 2011). Electrons in this region are distributed nonuniformly around the magnetic field (i.e., they are agyrotropic) (Aunai et al., 2013) and exhibit striated structures in velocity space (Bessho et al., 2014; Ng et al., 2011, 2012). Striations at progressively higher energies indicate the number of bounces in the current sheet and the amount of time exposed to the reconnection electric field. Acceleration is limited by cyclotron turning due to the normal magnetic field component (Chen et al., 2011), which results in ejection of electrons from the EDR.

Electrons enter the flux pileup region from the separatrices or from the vicinity of the EDR (Fu et al., 2006). High field line curvature in the vicinity of the EDR can scatter energetic electrons to higher pitch angles (Lavraud et al., 2016; Wang et al., 2010). Meanwhile, a parallel potential in the flux pileup region can trap these or other electrons with low parallel velocity entering from the separatrices (Egedal, Lê, Katz, et al., 2010; Egedal et al., 2008; Huang et al., 2015). As tension forces pull reconnected field lines away from the EDR, the shrinking field lines energize the plasma in the parallel direction through Fermi acceleration (Drake et al., 2009; Fu et al., 2006, 2011; Wu et al., 2013). Plasma jets compress the field in the $|B|_{min}$ region, energizing the trapped plasma in the perpendicular direction via betatron acceleration (Fu et al., 2006, 2011, 2013; Huang et al., 2015). Fermi and betatron acceleration are identified by cigar and pancake distribution functions, respectively, and can produce suprathermal electrons (Fu et al., 2011).

Energization during asymmetric reconnection (which is more typical at the MP) is somewhat different. Because the plasma temperatures and densities, and the magnetic field strengths are different in the MSH and MSP, the inflow stagnation point offsets from the *X* point (Cassak & Shay, 2007), and meandering MSH electrons can mix with gyrotropic inflowing MSP electrons to create agyrotropic distributions with a crescent shape (Hesse et al., 2014). Furthermore, the striations that form as a result of acceleration in the current layer are "V"-like instead of flat (Chen, Hesse, Wang, Bessho, et al., 2016). These findings suggest that the meandering motion and energization processes are different during asymmetric reconnection.

In situ observations of the EDR, finally made possible with the Magnetospheric Multiscale (MMS) mission (Burch et al., 2015; Torbert et al., 2014), confirmed the existence of perpendicular crescents and discovered parallel crescents in both antiparallel and guide field reconnection (Burch et al., 2016; Burch & Phan, 2016). These crescents exhibit cyclotron turning downstream from the EDR (Chen, Hesse, Wang, Gershman, et al., 2016), similar to the symmetric case (Chen et al., 2011). Such observations spurred a number of theories and models to explain the formation and structure of the crescent.

One- and two-dimensional theories as well as simulation results agree that crescents are formed by finite gyroradius effects of accelerated MSH particles mixing with the inflowing MSP plasma (Bessho et al., 2016; Egedal et al., 2016; Hesse et al., 2016; Shay et al., 2016). Near the X line, the asymmetric Hall electric field (Mozer, Angelopoulos, et al., 2008; Mozer et al., 2002; Mozer, Pritchett, et al., 2008) accelerates demagnetized MSH electrons into the magnetosphere. The associated electric potential acts as a filter that defines the shape of the crescent (Bessho et al., 2016; Egedal et al., 2016). Downstream, perpendicular crescents are turned toward the parallel direction by a finite normal magnetic field component along the Hall electric field (Shay et al., 2016). Demagnetization also occurs in the case of guide field reconnection as a result of strong field line curvature near the X line, allowing crescents to form (Hesse et al., 2016).

High time resolution distribution functions have allowed us to study particle acceleration within the EDR in greater detail, but why are the crescent distributions not more prevalent in MMS data or observed farther from the EDR? Furthermore, ions have been shown to be unresponsive to field variations at scale sizes larger than the ion inertial scale (Phan et al., 2016), yet electron distribution functions demonstrate structure below the electron inertial scales (Khotyaintsev et al., 2016). What role does this substructure play within the EDR?

In this paper, we attempt to answer both of these questions by examining the 16 December 2015 13:07:02 UT EDR encounter studied by Alm et al. (2017), Burch et al. (2016); Denton et al. (2016), Egedal et al. (2016),

Ergun, Goodrich, et al., 2016, Ergun et al. (2017), Shuster et al. (2017), Torbert et al. (2016), and others. We complement data from the Fast Plasma Instrument (FPI) with data from the Electron Drift Instrument (EDI), which is capable of measuring ambient flux up to 30 times faster (at select energies and pitch angles), in order to better understand agyrotropy on the ion and electron inertial scales.

2. Instrumentation

The Magnetospheric Multiscale (MMS) mission was launched on 13 March 2015 into an equatorial orbit with 1 R_E perigee, 12 R_E apogee and a 28.5° inclination. Its four identically instrumented satellites were designed to study electron-scale dynamics of magnetic reconnection at the magnetopause (Phase 1) and in the magnetotail (Phase 2). During the first dayside pass of Phase 1A, the mean interspacecraft separation was reduced to as little 10 km, or three electron inertial lengths. This small-scale separation and the unprecedented sampling rates of its particle instruments allow for investigation of electron kinetic effects that remain a large mystery of reconnection.

We present data from the FIELDS instrument suite (Torbert et al., 2015), including the fluxgate magnetometer (FGM) (Russell et al., 2014), electric field double probes (EDP) (Ergun et al., 2014; Lindqvist et al., 2014), and the Electron Drift Instrument (EDI) (Torbert et al., 2015). We also use data from the Fast Plasma Instrument (FPI) (Pollock et al., 2016). Data were captured at its highest resolution in the burst telemetry mode (Fuselier et al., 2016).

2.1. Moments of the Distribution

The Fast Plasma Instrument consists of four identical dual spectrometers spaced at 90° intervals around the spacecraft, allowing it to map the full distribution function independent of spacecraft spin, every 150 ms for ions and every 30 ms for electrons. Each distribution consists of 32 energy and 16 polar sweeps in four azimuthal deflections from each of the eight detectors. Data from one of the four azimuthal deflections on each detector can be used to compute moments of the distribution at 4 times the nominal rate, but at the expense of full velocity space coverage (Rager et al., 2017). We use 7.5 ms electron moments computed in such a manner to examine substructure of the electron diffusion region.

2.2. Electron Flux

The Electron Drift Instrument consists of two gun-detector units (GDUs) mounted on opposite sides of the spacecraft and facing opposite hemispheres. EDI can operate in one of two modes: ambient mode and electric field mode. In ambient mode, EDI detects electrons at selectable pitch angles and with energies of 250, 500, or 1,000 eV. In electric field mode, the gun fires modulated electron beams perpendicular to the magnetic field. When **B** and **E** are slowly varying so that the plasma is frozen-in, electrons in the beam undergo their normal cyclotron and $\mathbf{E}\times\mathbf{B}$ drift motions and return to the opposite GDU after one or more gyrations. The GDU scans for target directions that return beams (beam acquisition), and once they are detected, the scanning direction "windshield wipers," reversing repeatedly to track the target motion. Beams are assigned a quality of 0 to 3 based on their signal-to-noise ratio (SNR) and whether or not the time of flight was measured successfully. When the SNR is low, as is the case when no beams are returned and only ambient electrons enter the detector, a quality level of zero (Q0) is assigned. Throughout the time interval used in this study, EDI was in electric field mode.

The SNR is determined by correlating the electrons entering the detector with suitably delayed copies of the code that was imposed on the outgoing beam. The highest-quality beam within each 8 ms interval is retained. This sets the highest time resolution of Q0 data to 8 ms. One channel per GDU, however, is sampled unconstrained by the correlator mechanics. This datum, "data29," provides higher time resolution (1,024 S/s) observations at the expense of a defined data quality. Quality must be inferred from the lower time resolution quality flags, trends in count rates, transitions between windshield wiper and beam acquisition modes, and characteristics of the electric and magnetic fields.

In regions like the EDR, where **B** and **E** can fluctuate rapidly and $E_{||}$ can exist, the beam is typically scattered and does not return to the detector. Under these circumstances, there can be stretches of time during which few beams are detected and ambient electrons are reported as Q0 data. Consequently, the instrument remains in acquisition mode and scans the plane perpendicular to **B** (PA 90°) at a rate of 230°/s. This means that two

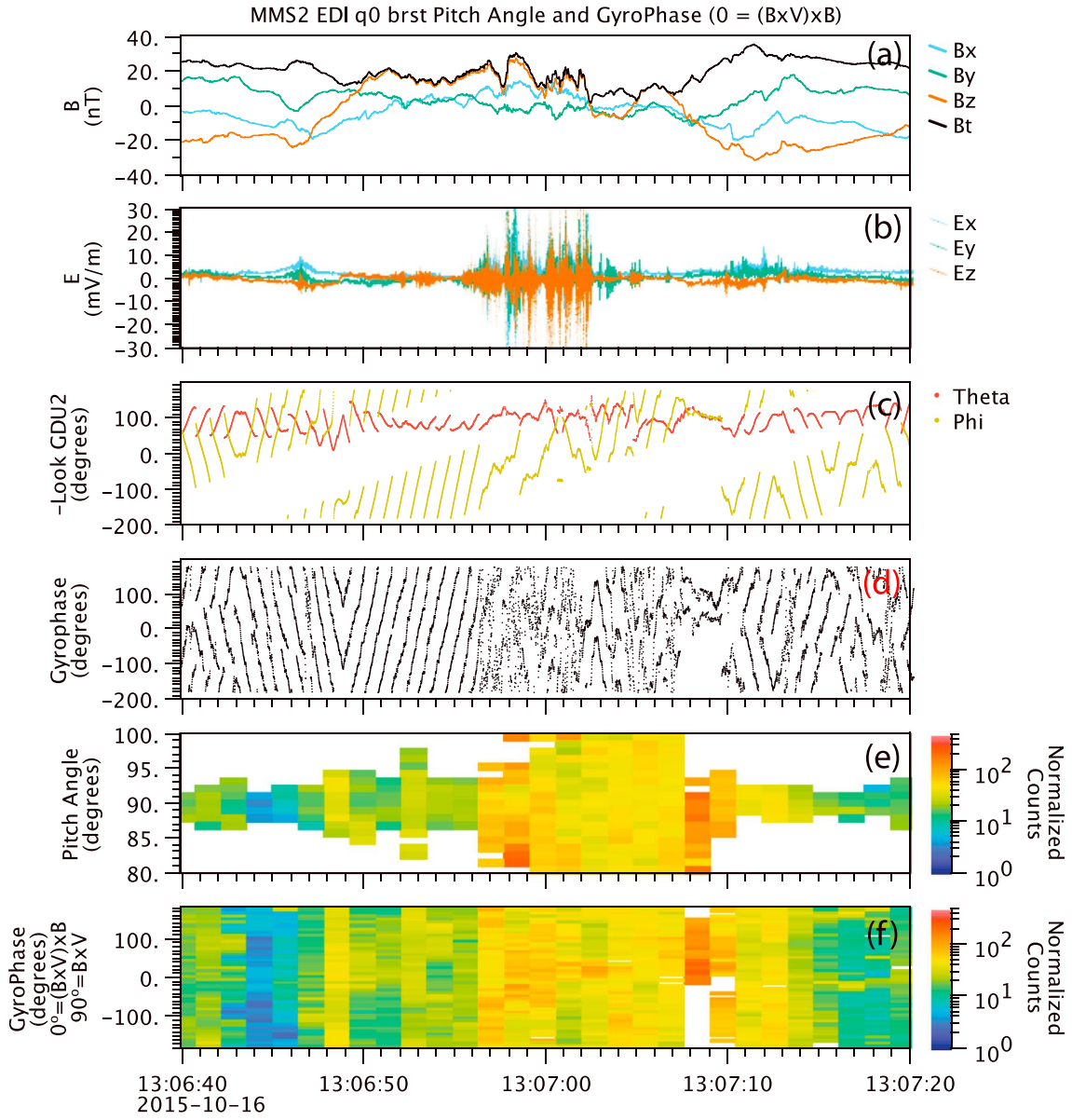


Figure 1. Overview of electron agyrotropy in the EDR as detected by the EDI instrument. The top three panels are the (a) magnetic and (b) electric fields, and (c) electron trajectories – taken to be opposite the nominal instrument look direction – in GSE coordinates. (d) The coverage of gyrophase from both GDUs. Counts are binned over 1.4 s, 1° PA, and 8° of gyrophase to produce (e) pitch angle and (f) gyrophase distributions for 500 eV electrons. Counts are normalized by the instrument dwell time in each angular bin in each 1.4 s interval.

GDUs facing opposite hemispheres can obtain full gyrophase distributions (GPDs) in 0.8 s. It also means that data29 can be used to analyze electron response to perpendicular electric fields within the EDR on millisecond time scales.

3. Event Overview

To study electron dynamics within the EDR of asymmetric reconnection, the MP crossing on 16 October 2015 is presented in Figure 1. The EDR encounter at 13:07:02 UT was originally identified by Burch et al. (2016) when the four MMS spacecraft detected the opening of magnetic field lines and strong energy dissipation. This region contained demagnetized electrons and was embedded within a larger ion diffusion region (Torbert et al., 2016). Closest approach (1.3 km) to the X line occurred at 13:07:02.35 by MMS4 (Denton et al., 2016). Figure 1a and 1b provide an overview of the magnetic and electric fields between 13:06:40 and 13:07:20 UT,

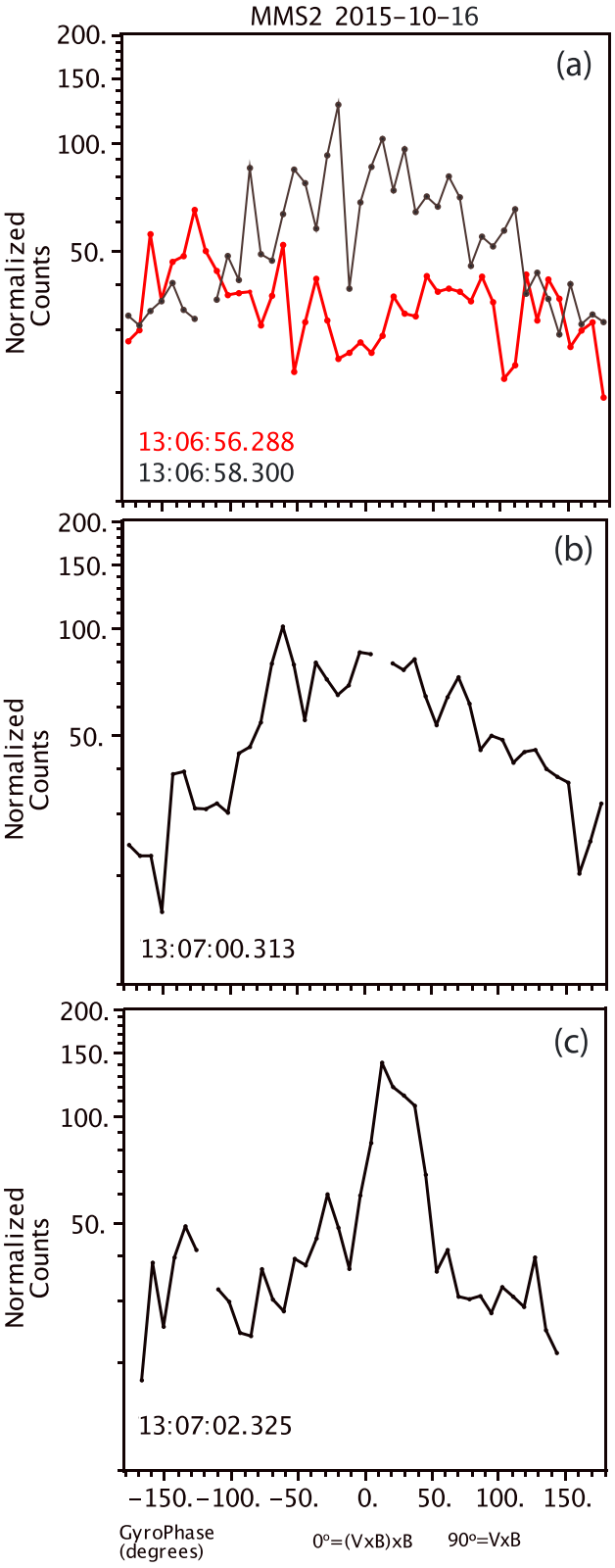


Figure 2. (a-c) EDI counts as a function of gyrophase, showing agyrotropy near 0° at three different times within the EDR. (a) A mostly isotropic background (red) is shown for comparison.

surrounding the EDR encounter. Electron trajectories (taken to be opposite to the nominal instrument look direction) of 500 eV electrons detected by GDU2 are represented as unit vectors in spherical GSE coordinates in Figure 1c. How such trajectories map to the gyrophase plane is depicted in Figure 1d. Zero degrees corresponds to the $(\mathbf{B} \times \mathbf{V}_e) \times \mathbf{B}$ direction ($\perp_1$), while 90° is the $\mathbf{B} \times \mathbf{V}_e$ direction ($\perp_2$), where $\mathbf{V}_e$ is the electron bulk velocity measured by FPI. Note that in Figure 1d, we have incorporated trajectories from both GDUs to show the completeness of gyrophase coverage. Careful examination of the angles in Figures 1c and 1d is important when determining data quality. Finally, the Q0 counts are binned over 1.4 s intervals, ~1° of PA (Figure 1e) and ~8° of gyrophase (Figure 1f). Counts are normalized by the fraction of time spent in each angular bin during each 1.4 s interval. An interval of 1.4 s was chosen as a compromise between EDI's rapid coverage of gyrophase and the slower time variability of observed agyrotropic structures.

At the edges of the intervals shown, from 13:06:40 to 13:06:48 UT and from 13:07:11 to 13:07:20, MMS2 is in the magnetosheath with $B_z < 0$. The plasma is frozen-in, which can be seen by the return beams detected by EDI near 0° and 180° in Figure 1f and the sudden shifts in incident angles (Figures 1c and 1d). After 13:06:48 until 13:06:56 UT, the magnetic field rotates and MMS2 crosses into the boundary layer on the MSP side of the MP. The weakened field causes EDI to lose its beam, evidenced by the smoothly varying incident angles (Figures 1c and 1d), and to sample the ambient plasma. Electron counts remain low ($\lesssim$ ~20) and gyrotropic (Figure 1f). At 13:06:57 UT, 90° PA counts rise from 30 to 80 (Figure 1e) and agyrotropy is visible starting at 13:06:58 UT (Figure 1f), with peaks centered on the $(\mathbf{B} \times \mathbf{V}_e) \times \mathbf{B}$ direction. This marks MMS2's entry into the EDR.

Agyrotropy is more visible in Figure 2. Vertical slices taken from Figure 1 show the transition from the fairly gyrotropic background outside the current layer (Figure 2a, red), to the agyrotropic configuration just 2 s later (Figure 2a, black). At 13:07:00.313 UT (Figure 2b), the distribution in the plane perpendicular to **B** is smoother and still centered around the $(\mathbf{B} \times \mathbf{V}_e) \times \mathbf{B}$ direction. Two seconds later (Figure 2c), the peak narrows and counts increase. This figure shows that the mechanism that heats the thermal population (~66 eV, shown later) and creates crescent shapes (Hesse et al., 2014; Burch et al., 2016) is effective at least up to 500 eV. It also shows that, at 500 eV, agyrotropy is observable with accumulation times of 1.4 s (590 electron cyclotron periods) and persists for several seconds.

4. Finite Larmor Radius Effects

EDI observations of persistent agyrotropy can be contrasted with the intervals in which crescent distributions are observed in 30 ms electron distribution functions (Burch et al., 2016; Burch & Phan, 2016; Chen, Hesse, Wang, Gershman, et al., 2016; Norgren et al., 2016). The crescent distribution, however, appears at energies much below 500 eV—typically around 60 eV. To understand why this is, we examine agyrotropy as a function of energy. One hope is that our results can be applied to missions with more limited capabilities. Cluster (Escoubet et al., 1997), for instance, has EDIs with capabilities similar to those of MMS, while its electron spectrometer samples every 4 s. Figure 3 presents FPI and EDI data for the EDR encounter on 16 December 2015. Depicted are gyrophase distributions for the cold and crescent populations (20 and 60 eV, respectively), as well as for three energy ranges that encompass the energies detectable by EDI: 250 eV,

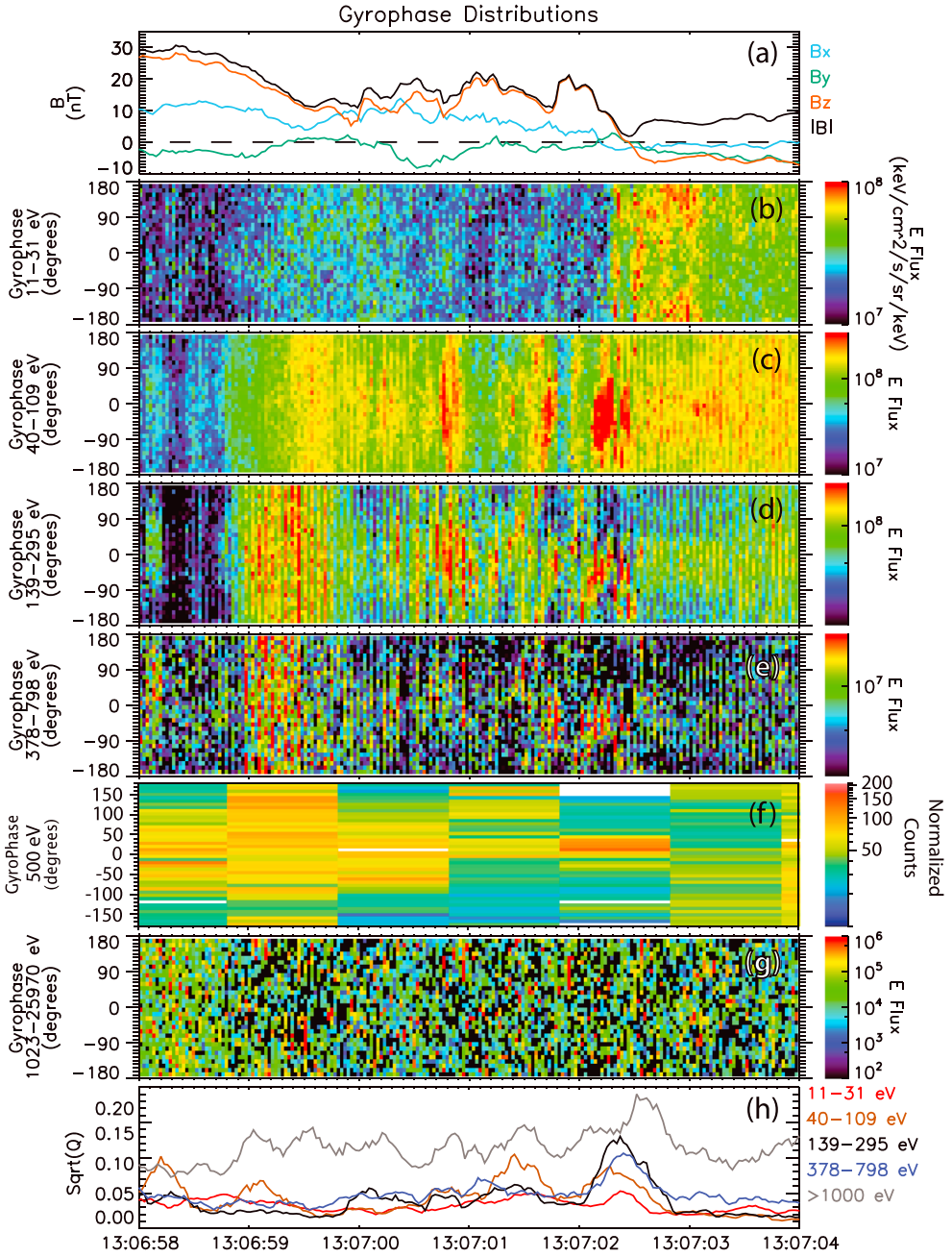


Figure 3. Gyrophase distributions showing how agyrotropy changes with energy. (a) The magnetic field provides context within the EDR for GPDs in six energy ranges: (b) 11–31 eV, (c) 40–109 eV, (d) 139–295 eV, (e) 378–798 eV, (f) 500 eV, and (g) ≥1 keV. Agyrotropy is more prominent in the 139–798 eV range (Figures 3d–3f) than the 11–109 eV range (Figures 3b and 3c). Above 1 keV, electron energy flux is sparse (Figure 3g), which leads to misleadingly (h) high levels of agyrotropy ($\sqrt{Q}$). The crescent population (Figure 3h, brown) has the most average levels of $\sqrt{Q}$, whereas the ~500 eV population (Figure 3h, blue) is, on average, the most agyrotropic.

500 eV, and 1 keV. We demonstrate that agyrotropy is visible farther from the X point and over longer time periods at higher energies.

Within the interval 13:06:58 to 13:07:04 UT, the 11–31 eV population (Figure 3b) is isotropic except for a brief interval after $|B|_{min}$ near ~13:07:02.4 UT, at which point it exhibits an enhancement at 180°, as opposed to the enhancement at 0° seen in the next energy channel (Figure 3c). Because the bulk velocity was not removed from the distribution function, the appearance of agyrotropy at such low energy could be caused by a drifting

population. The sign change is the result of a change in the orientation of B_z, and hence the coordinate system, as MMS2 crosses into the MSH. The 40–109 eV electron population (Figure 3c), which includes the crescent population, mostly exhibits an isotropic flux increase above background (e.g., 13:06:58.35 UT), with intense agyrotropy predominantly near $|B|_{\min}$. The next higher-energy range (Figure 3d) begins to highlight larger scale regions of agyrotropy. Flux for 139–295 eV electrons (Figure 3d) intensifies initially at 13:06:58.7 but then decreases nearly to background except in the gyrophase range of −90° to +90°, providing excellent contrast that highlights a 3.5 s interval of agyrotropy. Electrons in the 378–798 eV range (Figure 3e) exhibit the same tendency, made more obvious by the 1 s binned EDI Q0 counts in Figure 3f. Above ∼1 keV, flux is low and shows no tendency toward agyrotropy, an indication of the absence of meandering MSP electrons in the current layer. These results suggest that agyrotropy is more pronounced in the ∼250–500 eV energy range and can persist for as long as 3.5 s.

Figure 3h shows a scalar measure of agyrotropy: $\sqrt{Q}$, where $Q = \left(P_{xy}^2 + P_{xz}^2 + P_{yz}^2\right) / \left(P_{\perp}^2 + 2P_{\perp}P_{\parallel}\right)$ (Swisdak, 2016). Each trace is calculated over the subset of the pressure tensor corresponding to the energy ranges depicted in the GPDs, smoothed over 0.25 s. The >1,000 eV energy range exhibits a misleading amount of agyrotropy due to the sparseness of the data. The other energies summarize what is shown in the GPDs: 11–31 eV (red) is the most gyrotropic, 40–109 eV (brown) highlights key areas of agyrotropy, while 139–798 eV (black and blue) steadily rise starting just before 13:07:00 UT through the field reversal. We have also examined the quantities Agyrotropy (Scudder & Daughton, 2008) and the Degree of Nongyrotropy (Aunai et al., 2013), and each depicts qualitatively similar trends (not shown). Over the time interval shown, ∼500 eV electrons are the most consistently agyrotropic.

The spatial scale of agyrotropy can be determined if the velocity of the structure is known. During the interval 13:07:00 to 13:07:05 UT, the structure's velocity oscillated in the normal direction, but was constant along the outflow direction tangent to the MP, with a magnitude of −97 km/s (Denton et al., 2016). At 13:07:02.2 UT, a time studied in section 6, the normal component of the velocity was ∼ −40 km/s. The closest approach of MMS2 to the *X* point was ∼3 km at 13:07:02.47 UT, when $|B|_{\min}$ occurs (Denton et al., 2016). In addition, the average ion inertial length between 13:07:01 to 13:07:02 UT is $\lambda_i = 97$ km. Therefore, agyrotropy is observed ∼2.5 λ_i downstream from the *X* point and over a total distance of ∼3.5 λ_i.

Overall, the GPDs from EDI and FPI demonstrate agyrotropy that first appears at 500 eV 2.5 λ_i from the *X* point, then, as the spacecraft approaches the EDR, the agyrotropic crescent distribution appears at 66 eV in the vicinity of the EDR. This is consistent with finite gyroradius effects as MSH and MSP plasmas mix across the MP (Hesse et al., 2014; Norgren et al., 2016; Shay et al., 2016), meandering motion through the electron current sheet (Chen, Hesse, Wang, Gershman, et al., 2016), and diamagnetic effects (Egedal et al., 2016; Rager et al., 2017). These finite Larmor radius effects suggest that examining agyrotropy at 500 eV with EDI may help locate additional diffusion region encounters.

5. Electron Heating

Electron heating within the EDR can explain the observed evanescent nature of the crescent distribution as well as the persistent agyrotropy at higher energies. Outside of the EDR, 500 eV is in the tail of the energy flux distribution, while 60 eV is closer to the peak. As the plasma drifts into the EDR, it is heated, shifting the distribution to higher energy (Burch et al., 2016). The effects on agyrotropy are visible in Figure 4.

From ∼13:06:56 to 13:07:03 UT, during the period of enhanced magnetic and electric activity (Figure 4a), FPI detects perpendicular and parallel heating (Figure 4b). This is the same interval in which EDI observes increased perpendicular counts and gyrophase bunching (Figures 1e and 1f). Figure 4c shows the energy flux of 90° ± 15° PA electrons for the thermal population (taken to be ∼66 eV, the perpendicular electron temperature within the EDR) that exhibits crescent shapes, as well as for the three energy bins closest to the energies detectable by EDI: 230 eV, 485 eV, and 1,023 eV. The high temporal and spatial dependence of the crescent shapes can be understood by the fact that heating within the EDR shifts particle flux of 66 eV electrons into the low-energy tail of the distribution, decreasing the electron flux. Thus, averaging (or accumulating) over regions in which the background and heated plasmas mix will obscure the more tenuous crescent population in the data.

The opposite is true for higher energies. Flux of 90° PA electrons in the 230, 485, and 1,023 eV channels (Figure 4c), as well as the 500 eV EDI Q0 counts (4d), first begins to increase around 13:06:46 UT with the first

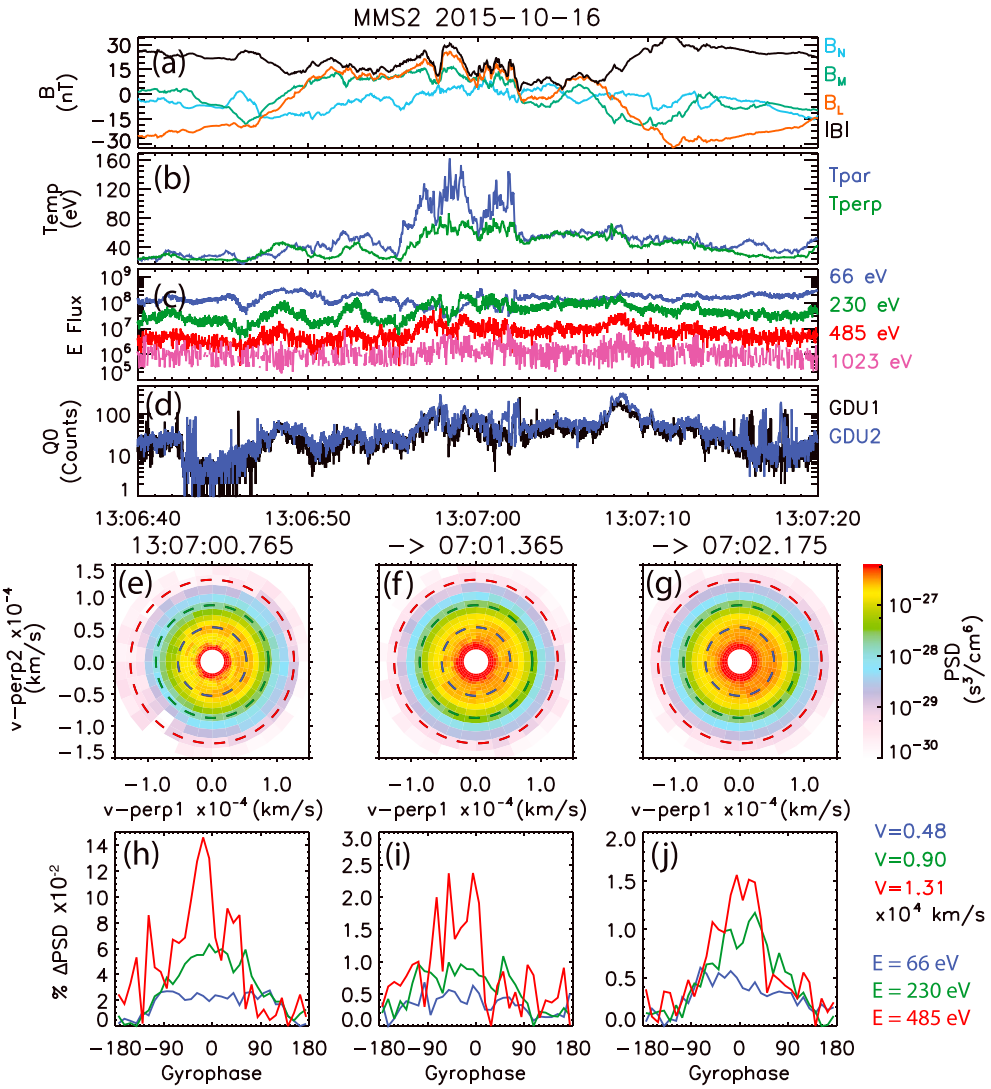


Figure 4. Evolution of electron energy flux and phase space density over time. From top to bottom, the (a) magnetic field, (b) electron perpendicular and parallel temperatures, (c) energy flux of 90° ± 15° PA electrons from FPI, and (d) 90° PA, 500 eV electron counts from EDI. Electron distribution functions with start time of 13:07:00.765 UT are averaged over (e) 0.03, (f) 0.6, (g) and 1.41 s. Concentric dashed circles mark the velocities corresponding to the energies shown in panel c (that of 1,023 eV is not shown due to poor counting statistics). (h–j) Gyrophase cuts around the distributions along the dashed circles are shown below the DFs. Overall, DFs show the crescent population is washed out over 1.41 s (Figure 4e and 4g), but anisotropy in 250 and 500 eV channels is more persistent.

magnetic field reversal. They gradually increase to their maximum values within the EDR before decreasing beyond the final B_z reversal at 13:07:09 UT. At times when EDI's GDUs face opposite directions, agyrotropy is occasionally visible directly from the difference in counts. This is the case at 13:07:02 UT and is the subject of Figure 5. The total change in FPI energy flux is nearly 1 order of magnitude, with 230 eV electron flux occasionally exceeding that of the thermal population (Figure˜4c). The flux of agyrotropic electrons is higher than the flux of gyrotropic, ambient electrons at the same energy, so the agyrotropy that develops within the EDR as a result of reconnection should be more prominent and persist for longer time intervals.

To demonstrate this point, we show distribution functions (DFs) averaged over time. DFs in the $v_{\perp 1}$-$v_{\perp 2}$ plane (Figures 4e–4g) reveal not only the crescent-shaped distribution at 66 eV but also agyrotropy in the 230 and 486 eV electrons. The DF in Figure 4e is a 30 ms sample taken at 13:07:00.765 UT, near when MMS2 entered the EDR. Concentric dashed circles at 0.48, 0.90, and 1.31×10^4 km/s draw attention to the phase space densities (PSD) of the corresponding 66, 230, and 485 eV electrons (1,023 eV is not shown due to poor

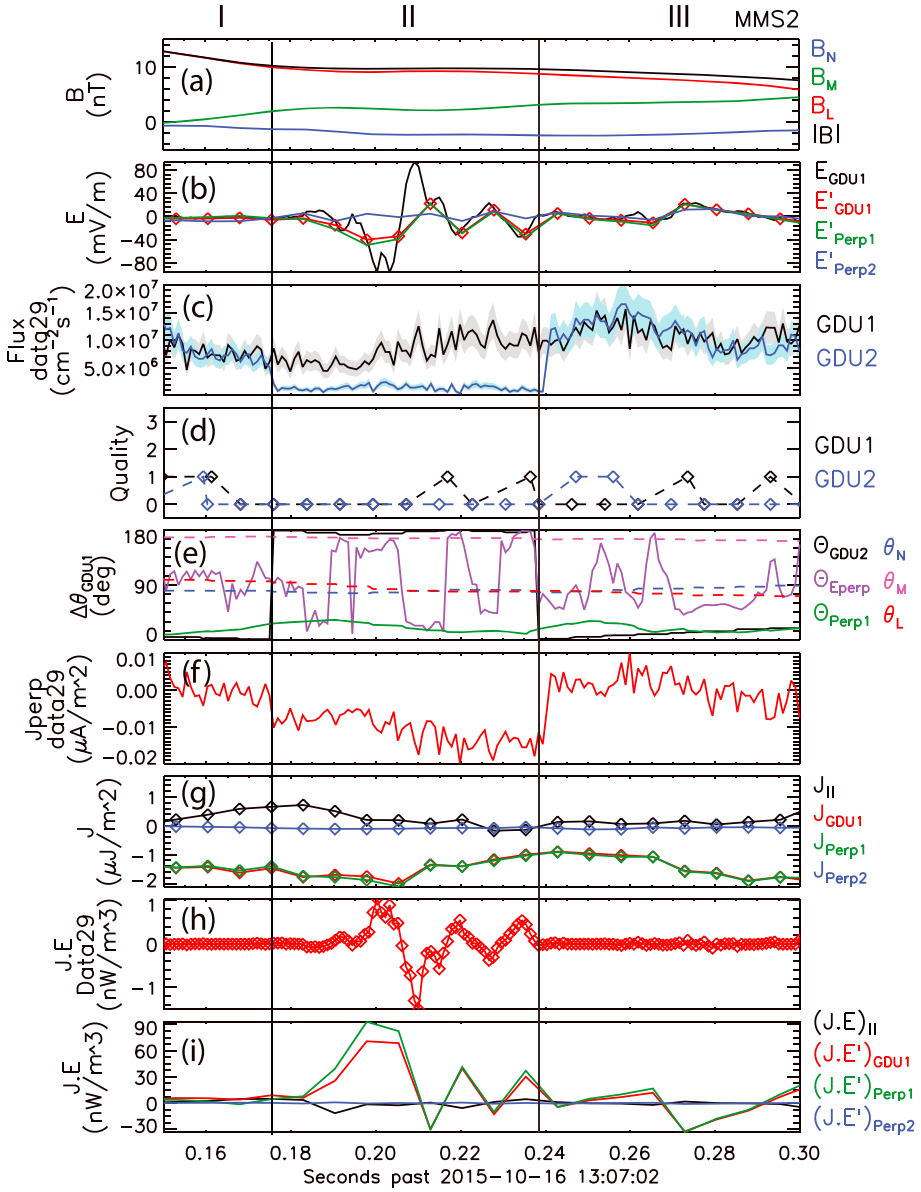


Figure 5. A view of electron response and dissipation over a 6.6 λ_e region surrounding the electron diffusion region. Quantities are shown on two time scale: 7.5 ms for FPI-derived quantities and 1 ms for EDI derived quantities. Two directions are highlighted: the $\perp_1$ direction in which the crescent distributions initially form and the GDU1 look direction. From top to bottom: (a) magnetic field; (b) electric field; (c) flux of 500 eV, 90° electrons, (d) beam quality, and (e) look angles from EDI; current density from (f) EDI and (g) FPI; and energy dissipation from (h) EDI and (i) FPI.

counting statistics). Below the distribution (Figures 4h–4j), we show cuts around the DFs along the concentric dashed circles, with the PSD normalized to reflect the percent change in PSD above the minimum value as a function of gyrophase angle. All four energy channels exhibit peaks near 0° gyrophase. That of 66 eV electrons (Figure 4h, blue) is plateau shaped, extending from approximately −140° to 140° with an overall 250% change in PSD. The agyrotropy of 230 eV electrons (Figure 4h, green) extends over the same range of gyrophase, has a rounded peak, and involves a 625% change in PSD. The energy channel closest to that of EDI Q0 counts shown in Figure 1 (485 eV) exhibits the largest change in PSD, nearly 1,500% (Figure 4h, red) and is skewed slightly toward the $-v_{\perp 2}$ direction, extending from ∼−180° to 75°. So, while agyrotropy was present in the 66, 230, and 485 eV channels, it is most pronounced near ∼500 eV.

We now average FPI distributions over 0.6 and 1.41 s (DFs; Figures 4f and 4i, and 4g and 4j, respectively) to demonstrate how these agyrotropies behave as the effective sampling time increases. While the DFs

themselves appear to become more gyrotropic (Figures 4f and 4g), the gyrophase plots (Figures 4i and 4j) show that only the relative difference between minimum and maximum PSD values decreases. For the crescent distribution, the relative change lowers to just ~50%, whereas the peaks corresponding to the 230 and 485 eV channels are more persistent, remaining at 100% and 150%, respectively, over 1.4 s. Electrons above 1 keV remain sparse with no obvious signs of agyrotropy, indicating that MSP electrons are not observed to meander on these time scales. While the crescent shape becomes barely visible due to the large dynamic range of the DF (Figure 4g), agyrotropy is prominent at the 230 and 485 eV over the course of 1.4 s (Figure 4j), in agreement with the EDI Q0 counts in Figure 1.

6. Microphysics of the EDR

As mentioned previously, the difference in counts between the GDUs can serve as a higher time resolution indicator of agyrotropy than the GPDs. When counts are calibrated into particle flux, the difference serves as an indicator of current density at the energy (500 eV) and pitch angle (90°) range of EDI. This can then be combined with the electric field to analyze energy dissipation. Figure 5 presents EDI and FPI observations for a 150 ms, or $6 \times 6.6\ \lambda_e$, interval surrounding the region of peak perpendicular energy dissipation identified in Burch et al. (2016).

To understand better how electrons in the current layer behave on time scales shorter than the cadence of electron distribution function captures, we look at 7.5 ms moments from FPI and 1 ms flux from EDI. The boundary normal coordinates in GSE are given by $\mathbf{e}_N = [0.820, 0.499, -0.281]$, $\mathbf{e}_M = [-0.481, 0.866, 0.135]$, $\mathbf{e}_L = [0.311, 0.024, 0.950]$, where $\mathbf{e}_N \times \mathbf{e}_M = \mathbf{e}_L$ (Denton et al., 2016). We focus on observations made in the plane perpendicular to **B**: namely, the $\perp_1$ and $\perp_2$ directions and along the trajectories of electrons incident on GDU1, $\mathbf{e}_{\mathrm{GDU1}}$. These directions relate to the *NML* system in the following way. For the subinterval described below, the average *N*, *M*, and *L* components of the magnetic field and electron bulk velocity are $\mathbf{B} = [-2.28, 2.35, 9.12]$ nT and $\mathbf{V}_e = [-112, -929, 88.7]$ km/s, respectively. With these, $\perp_1 = [-0.149, -0.966, 0.212]$ and $\perp_2 = [0.960, -0.091, 0.263]$. In addition, $\mathbf{e}_{\mathrm{GDU1}} = [0.1739, -0.9704, 0.1597]$. This can all be seen in Figure 5e, which plots the angle between $\mathbf{e}_{\mathrm{GDU1}}$ and other unit vectors. Thus, $\mathbf{e}_{\mathrm{GDU1}} \sim \perp_1 \sim -M$ and $\perp_2 \sim N$.

In Figure 5, we show the magnetic field in *NML* coordinates (Figure 5a). The electric field (Figure 5b) is in the spacecraft rest frame on EDI time scales (black) and in the electron rest frame ($\mathbf{E}' = \mathbf{E} + \mathbf{V}_e \times \mathbf{B}$) on FPI time scales (red, green, and blue). All *E* fields were linearly interpolated from EDP burst data onto EDI and FPI time tags. Figures 5c–5e show flux from both GDUs with measurement uncertainties given by the width of the grey and blue bars (Figure 5c); EDI beam quality (Figure 5d); and the angle between $\mathbf{e}_{\mathrm{GDU1}}$ and $\mathbf{e}_{\mathrm{GDU2}}$ (black), the perpendicular electric field (purple), the $\perp_1$ direction (green), and the *NML* coordinates (blue, magenta, and red, respectively; Figure 5e). Finally, we plot the current density from EDI, calculated as $J_{\mathrm{data29}} = q(f_{\mathrm{GDU1}} - f_{\mathrm{GDU2}})$ (*f* indicates electron flux and *q* is the electron charge), and FPI (Figure 5f and 5g), and the associated energy dissipation (Figure 5h and 5i). Data points are plotted as diamonds in some panels to demonstrate how well certain features are resolved on the two different time scales.

First, we note that the two GDUs operate independently from one another so that they do not always look in opposite directions. In regions I and III, which extend from 0.150 s to 0.176 s and from 0.237 s to 0.300 s, respectively, the GDUs are looking roughly in the same direction. During these intervals J_{data29} in Figure 5f does not indicate the difference in electron flow but, when combined with the flux values in Figure 5c, does provide an indication of how well the two GDUs are intercalibrated. In Region II, the intermediate interval from 0.176 s to 0.237 s (vertical solid lines), GDU2 flips to look opposite GDU1 and sees lower flux along the new direction. It is during this 0.061 s interval that Burch et al. (2016) observed the strongest energy dissipation and most prominent crescent distributions. The spatial scale of the interval is 2.4 λ_e along the normal direction and 5.9 λ_e along the outflow direction. We will focus on this interval, as measurements from EDI can be compared to those of FPI.

In Region II, the electric field at the 1 ms cadence (Figure 5b, black) is characterized by a large-amplitude (>80 mV/m) ~45 Hz wave. Superimposed on this field are ~20 mV/m oscillations with a period of 7 ms ($f \sim$ 148 Hz), roughly half the electron cyclotron frequency, which is $f_{\mathrm{ce}} = 280$ Hz in a 10 nT field. Thus, E_{GDU1} exhibits large-amplitude oscillations along the electron current layer. At 7.5 ms, the fluctuations along $\mathbf{e}_{\mathrm{GDU1}}$ (red) at $f_{\mathrm{ce}}/2$ are lost, while those at ~45 Hz are smoothed over and the amplitude is diminished. Fluctuations

and wave amplitude are similarly reduced along the $\perp_2$ direction (blue, compare with Figure 7a). $E'_{\perp 2}$ points normal to the current layer and contains the Hall field that accelerates the MSH population into the MSP.

As $\mathbf{e}_{GDU1}$ points tangent to the MP along the $-M$ direction, electrons detected by GDU1 are those flowing in the direction opposite to the reconnection electric field. The difference in flux between GDU1 (black) and GDU2 (blue) visible in Figure 5c indicates a net flow of electrons in the electron current layer. In Region II where the electric field oscillations occur, flux from GDU1 exhibits peaks with a frequency that is roughly $f_{ce}/2$. Interestingly, the large-amplitude waves at $f \sim 45$ Hz are not clearly visible in the flux measurements. However, the mean electric field, $E_{GDU1} = -11.9$ mV/m, gradually increases electron flux as it accelerates electrons along current sheet.

Flux profiles in Figure 5c result in a current (Figure 5f) in the $+M$ direction that intensifies throughout Region II. The current measured from the full distribution, J_{GDU1} (Figure 5g, red), also flows in the $+M$ direction and is modulated slightly by the large-amplitude electric field waves at 45 Hz. Current along the $\perp_2$ direction (Figure 5g, blue) is zero because of how the coordinate system is defined, while the parallel current (black) gradually decreases. The effect of the electric field on the current layer is a net flow of energy from the fields into the plasma (Figures 5h and 5i); the mean energy dissipation within Region II is $(J.E)_{GDU1} = 0.043\ \mathrm{nW/m^3}$ for 500 eV electrons and $(J.E')_{\perp 1} = 26\ \mathrm{nW/m^3}$ for the full distribution.

At this time, MMS2 was embedded in the electron current layer within the MSP just upstream from the X line as the X line passed from north to south (Denton et al., 2016). The electric field experienced large-amplitude fluctuations at $f \sim 45$ Hz and $f_{ce}/2$, which modulated the electron current layer. J_{GDU1} (Figures 5f and 5g, red) oscillates at both frequencies. A net electric field accelerates electrons in the $-M$ direction, intensifying the current of 500 eV electrons and producing an overall flow of energy from the fields into the plasma. Parallel currents (Figure 5g, black) reflect a gradually decreasing, monodirectional electron flow as the X line passes by. At the same time, MMS2 observes the Hall electric field $E'_{\perp 2}$, which can accelerates the energized MSH electrons into the MSP inflow region.

7. Wave Properties

Electric field oscillations such as those observed in the EDR are present on the MSP side of the EDR. Figure 6 presents wave power and polarization properties from 13:06:50 UT, just after MMS2 crossed into the MSP, to 13:07:10 UT, just after it exits back into the MSH, as indicated by the sign of B_L in Figure 6a. Figures 6b and 6c present spectrograms of electron flux from GDU1 and GDU2, while Figure 6d depicts electric field wave intensity. The black solid and dashed lines represent f_{ce} and $f_{ce}/2$, respectively. Each power spectral density estimate was computed using 0.25 s of data, a hamming window, and one-fourth overlap. Intense wave power at ~40 Hz between 13:06:55 and 13:07:03 UT is associated with a low-frequency oscillation in the current layer (Ergun, Holmes, et al., 2016) and is also visible in B_L. Wave intensity near f_{ce} first appears at 13:06:52 UT and continues intermittently until 13:07:03 UT, when MMS2 crosses into the MSH. The electron cyclotron frequency remains at or above EDI's Nyquist frequency until MMS2 enters the EDR, near 13:07:02 UT, at which time enhanced oscillations are observed. While broadband signatures appear in the electron flux spectrograms because of abrupt changes in flux associated with changes in the GDU look directions (see Figure 5c), there is an enhancement at ~148 Hz in both the electron flux and electric field within the EDR. This EDR interval will be examined in more detail below.

Polarization properties (Means, 1972; Rankin & Kurtz, 1970) of the electric field are given in Figures 6e–6h. They demonstrate the that waves near f_{ce} are strongly linearly polarized, with percent polarization >70% (Figure 6e) and ellipticity $\epsilon \sim 0$ (Figure 6e), where $\epsilon > 0$ (<0) indicates right- (left-) hand polarization. The waves also propagate perpendicular to the magnetic field with a wave normal angle of $\theta_k \sim 90°$ (Figure 6g) and have a coherency of ~0.75. Data in Figures 6d–6h that are less than 70% polarized have been removed. The magnetic field is devoid of similar wave activity (not shown), indicating that the waves are electrostatic in nature.

Electrostatic, linearly polarized, transverse wave activity correlates well with enhancements in the aygrotropy parameter $\sqrt{Q}$ in Figure 6i. All wave intervals leading up to the EDR are associated with at least modest increases in $\sqrt{Q}$, particularly in the 500 eV energy range (blue). The most intense waves are associated with the largest increases in $\sqrt{Q}$.

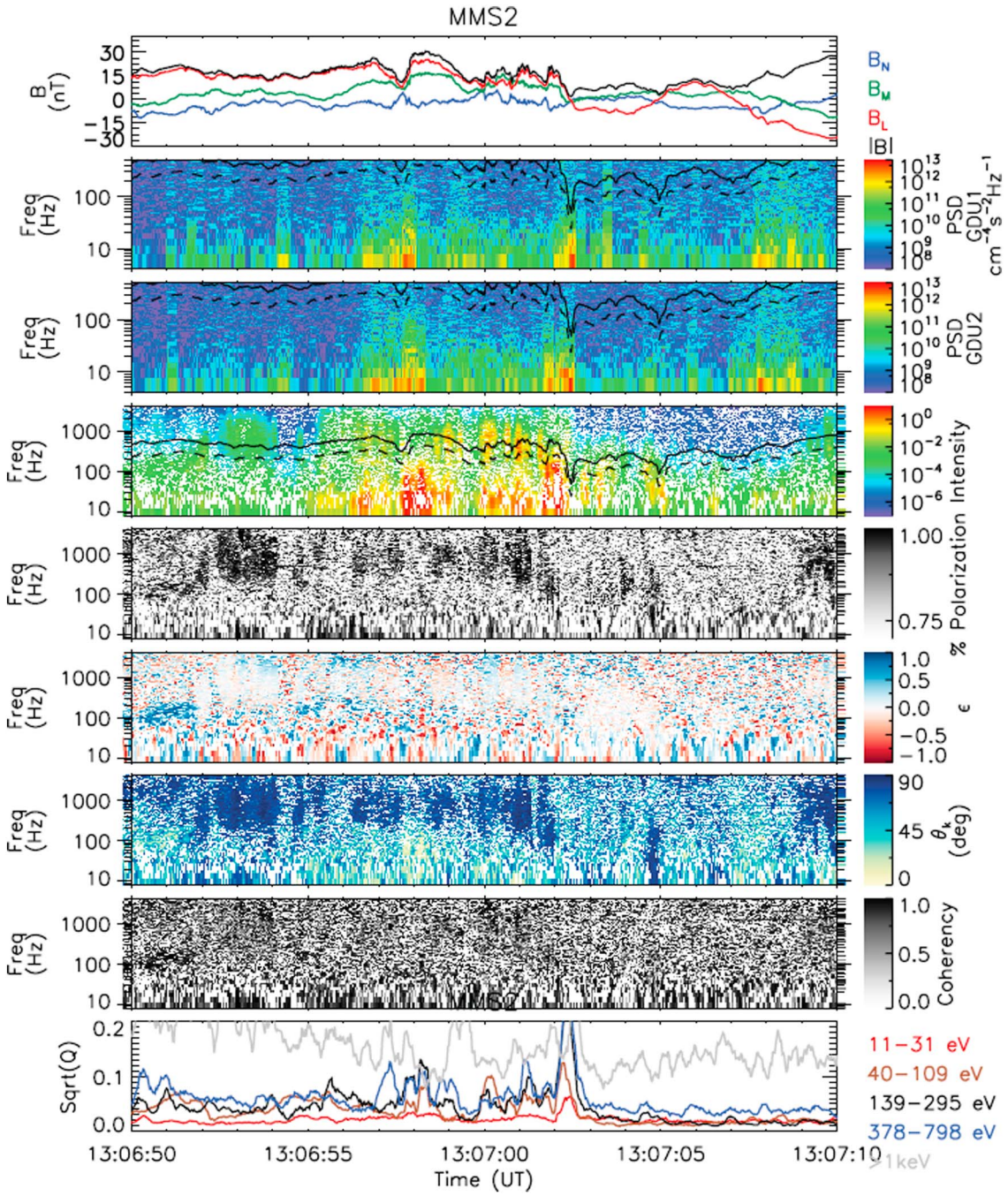


Figure 6. Wave power and polarization properties. Panels from top to bottom are (a) magnetic field in *NML* coordinates, (b and c) spectrograms of electron flux oscillations from GDU1 and GDU2, (d) electric field wave intensity, (e) percent polarization, (f) ellipticity, (g) wave normal angle, (h) coherency, and (i) the agyrotropy parameter $\sqrt{Q}$. Wave activity correlates with periods of enhanced agyrotropy.

We now return to the EDR interval examined in Figure 5 to more fully characterize the electric field and electron flux oscillations. The three components of the electric field in field-aligned coordinates are presented in Figure 7a. The EDP burst mode data have again been linearly interpolated onto EDI time tags. Oscillations in all three components are in-phase, suggesting that the wave is linearly polarized. This is better seen in the hodograms in Figures 7f and 7g, where **E** oscillates between quadrants I and III of the $\|$-$\perp_1$ plane. A minimum variance analysis was used to determine the wave normal direction (Fowler et al., 1967). For the interval outlined by the vertical dashed lines at 0.182 and 0.239 s in Figure 7a (which is also the interval in which the

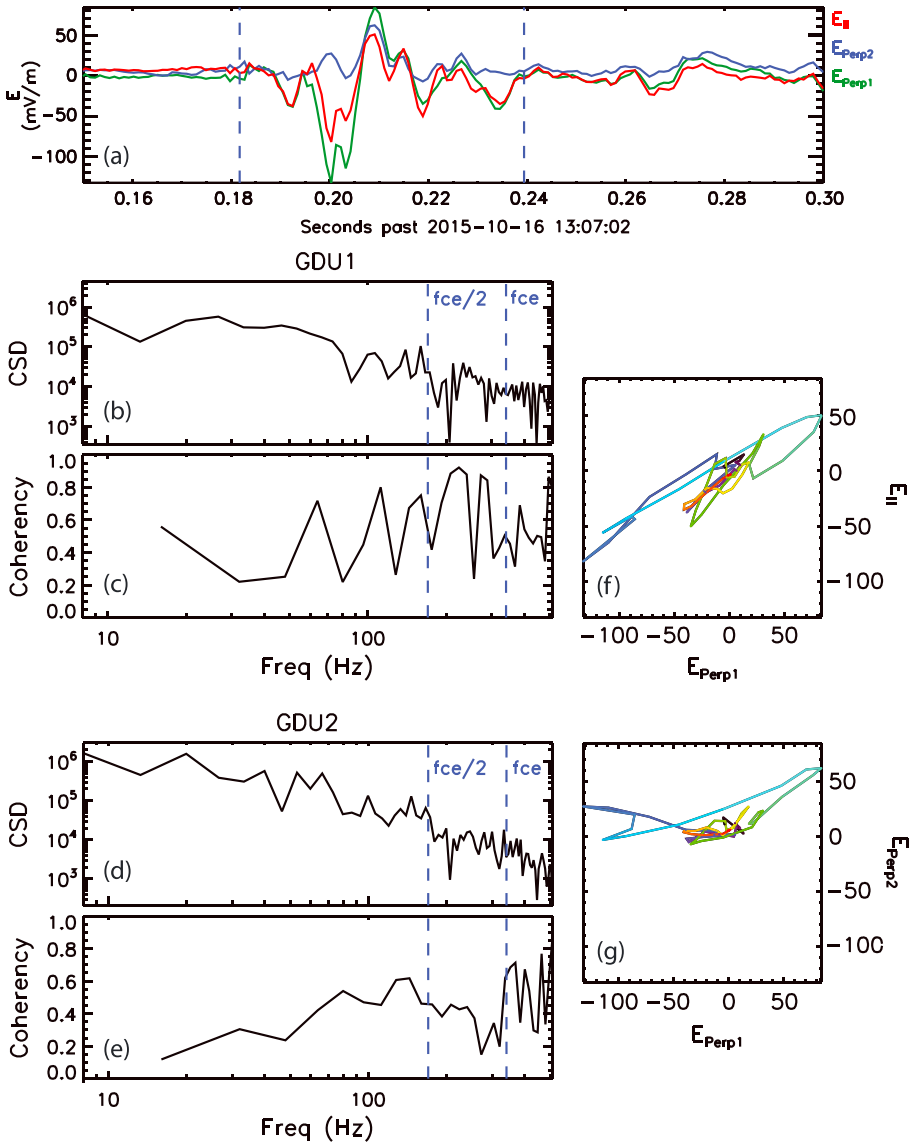


Figure 7. Properties of the electric field and electron flux oscillations within the EDR. (f and g) The electric field in Figure 7a is also plotted as hodograms. (b and c, and d and e) The cross-spectral density and cross coherence between E_{GDU1} and electron flux from GDU1 and GDU2, respectively, where E_{GDU1} is the electric field along the trajectories of electrons incident on GDU1. (a) Vertical dashed lines outline the hodogram and wave normal analysis interval, while those in Figures 7b–7e mark half and one times the electron cyclotron frequency.

hodograms were made), $\theta_{min} = 147°$ and $\mathbf{k}_{min} = [0.4332, 0.6619, -0.6111]$ in *NML* coordinates. The maximum variance direction tells us the oscillations lie along $\mathbf{k}_{max} = [-0.1021, 0.7081, 0.6977]$, in the *ML* plane.

The relationship between the oscillations in the electric field and electron flux can be seen the cross-spectral density (CSD) and cross coherence (Daly & Paschmann, 1998) in Figures 7b and 7c for GDU1 and Figures 7d and 7e for GDU2. The vertical dashed lines in each panel mark 0.5 and 1 times f_{ce}. The analysis interval included all of Region II from Figure 5 above, and the cross coherency was computed by averaging 0.0625 s sliding windows with one-fourth overlap. Both GDUs share a spectral component with the electric field just below $f_{ce}/2$, as noted by the slightly enhanced CSD in Figures 7b and 7d and peaks in coherency in Figure 7b and 7d. The signal is seen more clearly by GDU1.

Throughout MMS2's approach to the EDR, it observed linearly polarized electrostatic waves associated with increased agyrotropy. Within the EDR, where agyrotropy was most severe, wave power was also strongest.

The electrostatic oscillations influenced electrons flowing in the $\pm M$, or $\perp_1$ direction; the electron flux and electric field shared coherent spectral power signatures.

8. Discussion

We have shown that Q0 and data29 data products from EDI provide valuable insight into EDR dynamics. A word of caution is necessary, though. During the intervals 13:06:40 to 13:06:47 UT and 13:07:08 to 13:07:20 UT, the instrument look direction is steady or frequently changing directions (see Figures 1c and 1d). During these intervals, electron beams, visible as narrow intervals of high counts in Figure 4d and very narrow peaks in gyrophase in Figure 1f, contaminate the data. Despite the gyrophase plane orientation being confused by the fluctuating magnetic field and electron bulk velocity that define it, such narrow spikes are not visible within the EDR.

Theory and simulations argue that crescent distributions can form far from the X line (Egedal et al., 2016; Shay et al., 2016), yet they tend to be reported in situ only during brief intervals near the EDR (Burch et al., 2016; Khotyaintsev et al., 2016; Norgren et al., 2016). Both 1-D and 2-D theories, when applied to observed distribution functions, accurately predict the upper limit of the dense crescent population near 60 eV (Bessho et al., 2016; Egedal et al., 2016). Despite this, we have shown that agyrotropy is present up to 500 eV and that it is both more persistent and more prominent in higher-energy populations. Simulations depict a more realistic width of the agrytrotropic population, with the maximum and minimum velocities (energies) separated by a factor of 2–3 (4–9) (Shay et al., 2016). This is consistent with a factor of 7.5 separation between 66 eV and 500 eV.

Throughout the interval studied, MMS 1, 3, and 4 were separated from MMS2 by approximately 15 km, and each observed agyrotropy over similar time intervals. A multispacecraft timing analysis on the magnetic field gradient near 13:07:02 revealed the MP to be moving along its normal at ~45 km/s. If we assume a constant MP velocity, then the region of agyrotropy spans a total distance of ~160 km, or $1.7\lambda_i$ along the MP normal. However, the X line is being pushed in and out along the normal direction and is moving southward, tangent to the MP (Burch et al., 2016; Denton et al., 2016). Our analysis of agyrotropy as a function of energy revealed that the highest-energy electrons still trapped in the electron current layer is the 500 eV population. Their gyroradius, 3.6 km in a 15 nT field, provides an upper limit to the width of the EDR. This is consistent with a width of 2–3 km determined by Alm et al. (2017) via a 2-D parametric space mapping of the EDR.

Electron heating in the EDR causes particle flux of the electron crescent population to decrease while increasing particle flux at higher energies. Particle mixing as a result of reconnection, then, results in evanescent crescent shapes that identify the EDR at low energies, but persistent agyrotopy at higher energies. This finding could allow other missions that sample the MP with more limited particle detectors, such as the Time History of Events and Macroscale Interactions during Substorms (THEMIS) or Cluster missions, to observe EDR dynamics. Cluster also has EDIs with equivalent Q0 data at 8 ms (but does not have data29 at 1 ms) that can probe both long and short time scales. Note that distributions presented above were rotated into a field-aligned coordinate system. If the magnetic field rotates significantly throughout an accumulation interval, as can occur across the MP, the electron spectrometers will essentially smooth over gyrophase and fail to detect agyrotropy. EDI, however, operates in a field-aligned coordinate system and is thus more immune to rotations of the magnetic field.

As MMS2 approached the EDR on the MSP side, the electric field exhibited electrostatic, linearly polarized waves near 45 Hz and $f_{ce}/2$ with wave normal angle near $\theta_k = 90°$. The same region also exhibits significant wave power near the lower hybrid frequency ~45 Hz. Previous studies of the same event showed that the waves near 45 Hz are a type of drift wave that extend along the current layer and oscillate normal to it (Ergun et al., 2017), and that they are accompanied by large-amplitude parallel electric fields that may signal turbulent, patchy reconnection (Ergun et al., 2017; Ergun, Goodrich, et al., 2016). It has also been shown that $E_{||}$ may be generated by a two stream instability resulting from plasma mixing near the separatrix (Ergun, Holmes, et al., 2016). Here we showed a significant perpendicular component in-phase with $E_{||}$ and that the waves follow the electron gyrofrequency. It is possible that parallel electron beams drive an electrostatic whistler wave instability (Zhang et al., 1993) or that ring distributions excite electrostatic cyclotron harmonics (Kurth et al., 1979; Umeda et al., 2007). Wave occurrence and intensity correlated with increased agyrotropy, or regions where parallel crescents and ring distributions may form.

Within the EDR, electron flux along $\mathbf{e}_{GDU1}$ exhibits coherent spectral power near $f_{ce}/2$ simultaneous with the electrostatic waves. These oscillations result in variations along the primary electron current sheet. While instantaneous values of energy dissipation are large, energy is being transferred into and out of the plasma by waves so the overall dissipation is less. Still, when averaged over the wave activity, there is a net flow of energy from the fields into the plasma in the direction perpendicular to **B**. In an analysis of the generalized Ohm's law, the energy dissipation that results from considering all nonideal terms except $\eta\mathbf{J}^2$ accounts for only 50% of the total energy dissipated (Torbert et al., 2016). It is suggested that wave activity could account for at least part of the residual energy. Indeed, simulation show that wave turbulence produces a substantial amount of energy dissipation during 3-D reconnection (Fu et al., 2017).

9. Conclusions

We have used FPI and EDI to investigate the electron diffusion region on the ion and electron inertial scales, and as a function of energy. Gyrophase distributions displayed as a function of energy revealed that the 66 eV crescent population is short lived and appears primarily in the vicinity of the EDR. Meanwhile, agyrotropy at 250 and 500 eV is observed 2.5 λ_i downstream from the X point. Flux of 66 eV electrons drops within the EDR as the plasma is heated so that plasma mixing within the current layer obscures the crescent shape. Meanwhile, flux of 250 and 500 eV electrons increases within the EDR making agyrotropy at these energies more prominent. This is consistent with finite Larmor radius effect in the EDR.

Linearly polarized electrostatic waves were observed throughout the approach to and within the EDR. Wave occurrence and intensity correlated with increases in agyrotropy. Within the EDR, 7.5 ms resolution electron moments from FPI and electron flux at 1 ms resolution from EDI allowed us to investigate the substructure of reconnection. A large-amplitude drift wave near 45 Hz modulated the current density and energy dissipation from the entire distribution function. Superimposed on this was an electrostatic wave near $f_{ce}/2$ that shared coherent spectral power with modulations in the flux of 500 eV, 90° PA electrons. Fluctuations were directed along the electron current sheet, intensifying the current density and causing a net transfer of energy from the fields into the plasma. The occurrence of electrostatic waves within the EDR and along the separatrix where patchy reconnection is occurring may point to wave turbulence as a significant means of dissipating energy during reconnection.

Acknowledgments
We thank the successful MMS team for such wonderful data and NASA for its support via contract NNG04EB99C. IRAP contributions to MMS were supported by CNES. All MMS data are available through the MMS Science Data Center https://lasp.colorado.edu/mms/sdc/public/.

References

Alm, L., Argall, M. R., Torbert, R. B., Farrugia, C. J., Burch, J. L., Ergun, R. E., … Shuster, J. (2017). EDR signatures observed by MMS in the 16 October event presented in a 2-D parametric space. *Journal of Geophysical Research: Space Physics*, *122*, 3262–3276. https://doi.org/10.1002/2016JA023788

Aunai, N., Hesse, M., & Kuznetsova, M. (2013). Electron nongyrotropy in the context of collisionless magnetic reconnection. *Physics of Plasmas*, *20*(9), 092903. https://doi.org/https://doi.org/10.1063/1.4820953

Bessho, N., Chen, L.-J., Shuster, J. R., & Wang, S. (2014). Electron distribution functions in the electron diffusion region of magnetic reconnection: Physics behind the fine structures. *Geophysical Research Letters*, *41*, 8688–8695. https://doi.org/10.1002/2014GL062034

Bessho, N., Chen, L.-J., & Hesse, M. (2016). Electron distribution functions in the diffusion region of asymmetric magnetic reconnection. *Geophysical Research Letters*, *43*, 1828–1836. https://doi.org/10.1002/2016GL067886

Burch, J. L., & Phan, T. D. (2016). Magnetic reconnection at the dayside magnetopause: Advances with MMS. *Geophysical Research Letters*, *43*, 8327–8338. https://doi.org/10.1002/2016GL069787

Burch, J. L., Moore, T. E., Torbert, R. B., & Giles, B. L. (2015). Magnetospheric multiscale overview and science objectives. *Space Science Reviews*, *199*, 5–21. https://doi.org/10.1007/s11214-015-0164-9

Burch, J. L., Torbert, R. B., Phan, T. D., Chen, L.-J., Moore, T. E., Ergun, R. E., … Chandler, M. (2016). Electron-scale measurements of magnetic reconnection in space. *Science*, *352*, 6290. https://doi.org/10.1126/science.aaf2939

Cassak, P. A., & Shay, M. A. (2007). Scaling of asymmetric magnetic reconnection: General theory and collisional simulations. *Physics of Plasmas*, *14*(10), 102114. https://doi.org/10.1063/1.2795630

Chen, L.-J., Daughton, W. S., Lefebvre, B., & Torbert, R. B. (2011). The inversion layer of electric fields and electron phase-space-hole structure during two-dimensional collisionless magnetic reconnection. *Physics of Plasmas*, *18*(1), 012904. https://doi.org/10.1063/1.3529365

Chen, L.-J., Hesse, M., Wang, S., Bessho, N., & Daughton, W. (2016). Electron energization and structure of the diffusion region during asymmetric reconnection. *Geophysical Research Letters*, *43*, 452–461. https://doi.org/10.1002/2016GL068243

Chen, L.-J., Hesse, M., Wang, S., Gershman, D., Ergun, R., Pollock, C., … Avanov, L. (2016). Electron energization and mixing observed by MMS in the vicinity of an electron diffusion region during magnetopause reconnection. *Geophysical Research Letters*, *43*, 6036–6043. https://doi.org/10.1002/2016GL069215

Daly, P. W., & Paschmann, G. (1998). *Analysis methods for multi-spacecraft data*. Noordwijk, Netherlands: International Space Science Institute.

Denton, R. E., Sonnerup, B. U. Ö., Hasegawa, H., Phan, T. D., Russell, C. T., Strangeway, R. J., … Torbert, R. B. (2016). Motion of the MMS spacecraft relative to the magnetic reconnection structure observed on 16 October 2015 at 1307 UT. *Geophysical Research Letters*, *43*, 5589–5596. https://doi.org/10.1002/2016GL069214

Drake, J. F., Swisdak, M., Phan, T. D., Cassak, P. A., Shay, M. A., Lepri, S. T., … Zurbuchen, T. H. (2009). Ion heating resulting from pickup in magnetic reconnection exhausts. *Journal of Geophysical Research*, *114*, A05111. https://doi.org/10.1029/2008JA013701

Egedal, J., Fox, W., Katz, N., Porkolab, M., Øieroset, M., Lin, R. P., … Drake, J. F. (2008). Evidence and theory for trapped electrons in guide field magnetotail reconnection. *Journal of Geophysical Research*, *113*, A12207. https://doi.org/10.1029/2008JA013520

Egedal, J., Lê, A., Katz, N., Chen, L.-J., Lefebvre, B., Daughton, W., & Fazakerley, A. (2010). Cluster observations of bidirectional beams caused by electron trapping during antiparallel reconnection. *Journal of Geophysical Research*, *115*, A03214. https://doi.org/10.1029/2009JA014650

Egedal, J., Lê, A., Zhu, Y., Daughton, W., Øieroset, M., Phan, T., Lin, R. P., & Eastwood, J. P. (2010). Cause of super-thermal electron heating during magnetotail reconnection. *Geophysical Research Letters*, *37*, L10102. https://doi.org/10.1029/2010GL043487

Egedal, J., Le, A., Daughton, W., Wetherton, B., Cassak, P. A., Chen, L.-J., … Avanov, L. A. (2016). Spacecraft observations and analytic theory of crescent-shaped electron distributions in asymmetric magnetic reconnection. *Physical Review Letters*, *117*(18), 185101. https://doi.org/10.1103/PhysRevLett.117.185101

Ergun, R. E., Tucker, S., Westfall, J., Goodrich, K. A., Malaspina, D. M., Summers, D., … Cully, C. M. (2014). The axial double probe and fields signal processing for the MMS mission. *Space Science Reviews*, *199*(1), 167–188. https://doi.org/10.1007/s11214-014-0115-x

Ergun, R. E., Goodrich, K. A., Wilder, F. D., Holmes, J. C., Stawarz, J. E., Eriksson, S., … Marklund, G. (2016). Magnetospheric multiscale satellites observations of parallel electric fields associated with magnetic reconnection. *Physical Review Letters*, *116*(23), 235102. https://doi.org/10.1103/PhysRevLett.116.235102

Ergun, R. E., Holmes, J. C., Goodrich, K. A., Wilder, F. D., Stawarz, J. E., & Eriksson, S. (2016). Magnetospheric Multiscale observations of large-amplitude, parallel, electrostatic waves associated with magnetic reconnection at the magnetopause. *Geophysical Research Letters*, *43*, 5626–5634. https://doi.org/10.1002/2016GL068992

Ergun, R. E., Chen, L.-J., Wilder, F. D., Ahmadi, N., Eriksson, S., Usanova, M. E., … Wang, S. 2017). Drift waves, intense parallel electric fields, and turbulence associated with asymmetric magnetic reconnection at the magnetopause. *Geophysical Research Letters*, *44*, 2978–2986. https://doi.org/10.1002/2016GL072493

Escoubet, C. P., Schmidt, R., & Russell, C. (1997). *The Cluster and PHOENIX missions, Space Science Reviews*. Dordrecht: Kluwer Academic.

Fowler, R. A., Kotick, B. J., & Elliott, R. D. (1967). Polarization analysis of natural and artificially induced geomagnetic micropulsations. *Journal of Geophysical Research*, *72*(11), 2871–2883. https://doi.org/10.1029/JZ072i011p02871

Fu, H. S., Khotyaintsev, Y. V., André, M., & Vaivads, A. (2011). Fermi and betatron acceleration of suprathermal electrons behind dipolarization fronts. *Geophysical Research Letters*, *38*, L16104. https://doi.org/10.1029/2011GL048528

Fu, H. S., Khotyaintsev, Y. V., Vaivads, A., Retino, A., & Andre, M. (2013). Energetic electron acceleration by unsteady magnetic reconnection. *Nature Physics*, *9*(7), 426–430.

Fu, H. S., Vaivads, A., Khotyaintsev, Y. V., André, M., Cao, J. B., Olshevsky, V., Eastwood, J. P., & Retinò, A. (2017). Intermittent energy dissipation by turbulent reconnection. *Geophysical Research Letters*, *44*, 37–43. https://doi.org/10.1002/2016GL071787

Fu, X. R., Lu, Q. M., & Wang, S. (2006). The process of electron acceleration during collisionless magnetic reconnection. *Physics of Plasmas*, *13*(1), 12309. https://doi.org/10.1063/1.2164808

Fuselier, S. A., Lewis, W. S., Schiff, C., Ergun, R., Burch, J. L., Petrinec, S. M., & Trattner, K. J. (2016). Magnetospheric multiscale science mission profile and operations. *Space Science Reviews*, *199*, 77–103. https://doi.org/10.1007/s11214-014-0087-x

Graham, D. B., Khotyaintsev, Y. V., Vaivads, A., André, M., & Fazakerley, A. N. (2014). Electron dynamics in the diffusion region of an asymmetric magnetic reconnection. *Physical Review Letters*, *112*(21), 215004. https://doi.org/10.1103/PhysRevLett.112.215004

Hesse, M., Aunai, N., Sibeck, D., & Birn, J. (2014). On the electron diffusion region in planar, asymmetric, systems. *Geophysical Research Letters*, *41*, 8673–8680. https://doi.org/10.1002/2014GL061586

Hesse, M., Liu, Y.-H., Chen, L.-J., Bessho, N., Kuznetsova, M., Birn, J., & Burch, J. L. (2016). On the electron diffusion region in asymmetric reconnection with a guide magnetic field. *Geophysical Research Letters*, *43*, 2359–2364. https://doi.org/10.1002/2016GL068373

Huang, C., Lu, Q., & Wang, S. (2010). The mechanisms of electron acceleration in antiparallel and guide field magnetic reconnection. *Physics of Plasmas*, *17*(7), 72306. https://doi.org/10.1063/1.3457930

Huang, C., Wu, M., Lu, Q., Wang, R., & Wang, S. (2015). Electron acceleration in the dipolarization front driven by magnetic reconnection. *Journal of Geophysical Research: Space Physics*, *120*, 1759–1765. https://doi.org/10.1002/2014JA020918

Khotyaintsev, Y. V., Graham, D. B., Norgren, C., Eriksson, E., Li, W., Johlander, A., … Burch, J. L. (2016). Electron jet of asymmetric reconnection. *Geophysical Research Letters*, *43*, 5571–5580. https://doi.org/10.1002/2016GL069064

Kurth, W. S., Craven, J. D., Frank, L. A., & Gurnett, D. A. (1979). Intense electrostatic waves near the upper hybrid resonance frequency. *Journal of Geophysical Research*, *84*(A8), 4145–4164. https://doi.org/10.1029/JA084iA08p04145

Lavraud, B., Zhang, Y. C., Vernisse, Y., Gershman, D. J., Dorelli, J., Cassak, P. A., … Yokota, S. (2016). Currents and associated electron scattering and bouncing near the diffusion region at Earth's magnetopause. *Geophysical Research Letters*, *43*, 3042–3050. https://doi.org/10.1002/2016GL068359

Lindqvist, P.-A., Olsson, G., Torbert, R. B., King, B., Granoff, M., Rau, D., … Tucker, S. (2014). The spin-plane double probe electric field instrument for MMS. *Space Science Reviews*, *199*(1), 137–165. https://doi.org/10.1007/s11214-014-0116-9

Means, J. D. (1972). Use of the three-dimensional covariance matrix in analyzing the polarization properties of plane waves. *Journal of Geophysical Research*, *77*(28), 5551–5559. https://doi.org/10.1029/JA077i028p05551

Mozer, F. S., Angelopoulos, V., Bonnell, J., Glassmeier, K. H., & McFadden, J. P. (2008). THEMIS observations of modified Hall fields in asymmetric magnetic field reconnection. *Geophysical Research Letters*, *35*, L17S04. https://doi.org/10.1029/2007GL033033

Mozer, F. S., Bale, S. D., & Phan, T. D. (2002). Evidence of diffusion regions at a subsolar magnetopause crossing. *Physical Review Letters*, *89*(1), 15002. https://doi.org/10.1103/PhysRevLett.89.015002

Mozer, F. S., Pritchett, P. L., Bonnell, J., Sundkvist, D., & Chang, M. T. (2008). Observations and simulations of asymmetric magnetic field reconnection. *Journal of Geophysical Research*, *113*, A00C03. https://doi.org/10.1029/2008JA013535

Ng, J., Egedal, J., Le, A., Daughton, W., & Chen, L.-J. (2011). Kinetic structure of the electron diffusion region in antiparallel magnetic reconnection. *Physical Review Letters*, *106*(6), 65002. https://doi.org/10.1103/PhysRevLett.106.065002

Ng, J., Egedal, J., Le, A., & Daughton, W. (2012). Phase space structure of the electron diffusion region in reconnection with weak guide fields. *Physics of Plasmas*, *19*, 112108. https://doi.org/10.1063/1.4766895

Norgren, C., Graham, D. B., Khotyaintsev, Y. V., André, M., Vaivads, A., Chen, L.-J., … Burch, L. (2016). Finite gyroradius effects in the electron outflow of asymmetric magnetic reconnection. *Geophysical Research Letters*, *43*, 6724–6733. https://doi.org/10.1002/2016GL069205

Phan, T. D., Eastwood, J. P., Cassak, P. A., Øieroset, M., Gosling, J. T., Gershman, D. J., … Wilder, F. D. (2016). MMS observations of electron-scale filamentary currents in the reconnection exhaust and near the X line. *Geophysical Research Letters*, *43*, 6060–6069. https://doi.org/10.1002/2016GL069212

Pollock, C., Moore, T., Jacques, A., Burch, J., Gliese, U., Saito, Y., … Zeuch, M. (2016). Fast Plasma Investigation for magnetospheric multiscale. *Space Science Reviews*, *199*(1), 331–406. https://doi.org/10.1007/s11214-016-0245-4

Rager, A., Dorelli, J., Gershman, D., Avanov, L., Torbert, R., Burch, J., … Saito, Y. (2017). Electron crescent distributions as a manifestation of diamagnetic drift in an electron scale current sheet. arXiv:1706.08435v3 [physics.space-ph]

Rankin, D., & Kurtz, R. (1970). Statistical study of micropulsation polarizations. *Journal of Geophysical Research*, *75*(28), 5444–5458. https://doi.org/10.1029/JA075i028p05444

Russell, C. T., Anderson, B. J., Baumjohann, W., Bromund, K. R., Dearborn, D., Fischer, D., … Richter, I. (2014). The magnetospheric multiscale magnetometers. *Space Science Reviews*, *199*(1), 189–256. https://doi.org/10.1007/s11214-014-0057-3

Scudder, J., & Daughton, W. (2008). "Illuminating" electron diffusion regions of collisionless magnetic reconnection using electron agyrotropy. *Journal of Geophysical Research*, *113*, A06222. https://doi.org/10.1029/2008JA013035

Shay, M. A., Phan, T. D., Haggerty, C. C., Fujimoto, M., Drake, J. F., Malakit, K., … Swisdak, M. (2016). Kinetic signatures of the region surrounding the X line in asymmetric (magnetopause) reconnection. *Geophysical Research Letters*, *43*, 4145–4154. https://doi.org/10.1002/2016GL069034

Shuster, J. R., Argall, M. R., Torbert, R. B., Chen, L.-J., Farrugia, C. J., Alm, L., … Pollock, C. J. (2017). Hodographic approach for determining spacecraft trajectories through magnetic reconnection diffusion regions. *Geophysical Research Letters*, *44*, 1625–1633. https://doi.org/10.1002/2017GL072570

Speiser, T. W. (1965). Particle trajectories in model current sheets: 1. Analytical solutions. *Journal of Geophysical Research*, *70*(17), 4219–4226. https://doi.org/10.1029/JZ070i017p04219

Swisdak, M. (2016). Quantifying gyrotropy in magnetic reconnection. *Geophysical Research Letters*, *43*, 43–49. https://doi.org/10.1002/2015GL066980

Torbert, R. B., Russell, C. T., Magnes, W., Ergun, R. E., Lindqvist, P.-A., LeContel, O., … Lappalainen, K. (2014). The FIELDS instrument suite on MMS: Scientific objectives, measurements, and data products. *Space Science Reviews*, *199*(1), 105–135. https://doi.org/10.1007/s11214-014-0109-8

Torbert, R. B., Vaith, H., Granoff, M., Widholm, M., Gaidos, J. A., Briggs, B. H., … Kooi, V. (2015). The electron drift instrument for MMS. *Space Science Reviews*, *199*(1), 283–305. https://doi.org/10.1007/s11214-015-0182-7

Torbert, R. B., Burch, J. L., Giles, B. L., Gershman, D., Pollock, C. J., Dorelli, J., … Bounds, S. (2016). Estimates of terms in Ohm's law during an encounter with an electron diffusion region. *Geophysical Research Letters*, *43*, 5918–5925. https://doi.org/10.1002/2016GL069553

Umeda, T., Ashour-Abdalla, M., Schriver, D., Richard, R. L., & Coroniti, F. V. (2007). Particle-in-cell simulation of Maxwellian ring velocity distribution. *Journal of Geophysical Research*, *112*, A04212. https://doi.org/10.1029/2006JA012124

Wang, R., Lu, Q., Huang, C., & Wang, S. (2010). Multispacecraft observation of electron pitch angle distributions in magnetotail reconnection. *Journal of Geophysical Research*, *115*, A01209. https://doi.org/10.1029/2009JA014553

Wu, M., Lu, Q., Volwerk, M., Vörös, Z., Zhang, T., Shan, L., & Huang, C. (2013). A statistical study of electron acceleration behind the dipolarization fronts in the magnetotail. *Journal of Geophysical Research: Space Physics*, *118*, 4804–4810. https://doi.org/10.1002/jgra.50456

Zhang, Y. L., Matsumoto, H., & Omura, Y. (1993). Linear and nonlinear interactions of an electron beam with oblique whistler and electrostatic waves in the magnetosphere. *Journal of Geophysical Research*, *98*(A12), 21,353–21,363. https://doi.org/10.1029/93JA01937